Inorganic Chemistry

Article

pubs.acs.org/IC

Synthesis, Structure, Multiband Optical, and Electrical Conductive Properties of a 3D Open Cubic Framework Based on $[Cu_8Sn_6S_{24}]^{z-}$ Clusters

Xian Zhang,[†,‡] Qiuran Wang,[†,‡] Zhimin Ma,[†,‡] Jianqiao He,[§] Zhe Wang,[∥] Chong Zheng,[⊥] Jianhua Lin,[†] and Fuqiang Huang*[,†,§]

[†]Beijing National Laboratory for Molecular Sciences and State Key Laboratory of Rare Earth Materials Chemistry and Applications, College of Chemistry and Molecular Engineering, Peking University, 202 Chengfu Road, Beijing 100871, P. R. China

[§]CAS Key Laboratory of Materials for Energy Conversion, Shanghai Institute of Ceramics, Chinese Academy of Sciences, 1295 Dingxi Road, Shanghai 200050, P. R. China

[∥]School of Physics and Nuclear Energy Engineering, Beihang University, Xueyuan Road, Haidian District, Beijing 100191, P. R. China

[⊥]Department of Chemistry and Biochemistry, Northern Illinois University, DeKalb, Illinois 60115, United States

Supporting Information

ABSTRACT: Two compounds with the formulas of $Na_4Cu_{32}Sn_{12}S_{48}\cdot 4H_2O$ and $K_{11}Cu_{32}Sn_{12}S_{48}\cdot 4H_2O$ were synthesized via flux (with thiourea as reactive flux) and hydrothermal method, respectively. The black crystals of $Na_4Cu_{32}Sn_{12}S_{48}\cdot 4H_2O$ and $K_{11}Cu_{32}Sn_{12}S_{48}\cdot 4H_2O$ both crystallize in the cubic space group of $Fm\bar{3}c$ with the cell constants a = 17.921(2) Å and a = 18.0559(6) Å, respectively. The crystal structures feature a 3D open-framework with the unique $[Cu_8Sn_6S_{24}]^{z-}$ (z = 13 for $Na_4Cu_{32}Sn_{12}S_{48}\cdot 4H_2O$; z = 14.75 for $K_{11}Cu_{32}Sn_{12}S_{48}\cdot 4H_2O$) clusters acting as building blocks. The $[Cu_8Sn_6S_{24}]^{z-}$ cluster of the T_h symmetry is built up by eight $[CuS_3]$ triangles and six $[SnS_4]$ tetrahedra. The powder samples were investigated by X-ray diffraction and optical absorption measurements. Both phase-pure compounds show multiabsorption character with a main absorption edge (2.0 eV for $Na_4Cu_{32}Sn_{12}S_{48}\cdot 4H_2O$ and 1.9 eV for $K_{11}Cu_{32}Sn_{12}S_{48}\cdot 4H_2O$) and an additional absorption peak (1.61 eV for $Na_4Cu_{32}Sn_{12}S_{48}\cdot 4H_2O$ and 1.52 eV for $K_{11}Cu_{32}Sn_{12}S_{48}\cdot 4H_2O$), which are perfectly consistent with the first-principle calculation results. The analyses of the density of states further reveal that the two optical absorption bands in each compound are attributed to the two transitions of Cu-3d-S-3p → Sn-5s. The multiband nature of two compounds also enhances photocatalytic activity under visible light irradiation, with which the degradation of methyl blue over $Na_4Cu_{32}Sn_{12}S_{48}\cdot 4H_2O$ reached 100% in 3 h. The 3D open-framework features also facilitate the ionic conductivity nature of the $Na_4Cu_{32}Sn_{12}S_{48}\cdot 4H_2O$ compound, which achieved ~10^{-5} S/cm at room temperature.

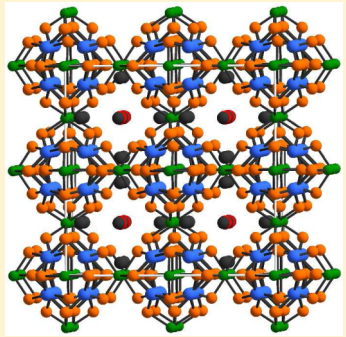

INTRODUCTION

Multifunctional materials with increasingly complex compositions have received much attention in recent years due to their fascinating structures, which are constructed by naturally formed structural/functional units from different bonding and packing habits of different elements, and due to their potential applications in many different areas. It is believed that the structural/functional units can reflect different electronic structure and physical properties from the parental simple binary and ternary compounds.[1−5] Then the combined properties can produce the desired multifunctional materials by selecting proper structural/functional units.

Chalcogenides as a large family of compounds always have complex structures and rich chemical/physical properties. Among these compounds, 3D open-framework or zeolite-like chalcogenides have many intriguing architectures,[6−8] topologies and potential applications in the fields of photoluminescence,[6,9] photocatalysis,[10,11] nonlinear optical response,[12] selective ion-exchange,[13−17] and low temperature fast-ion conductors.[7] In contrast to oxygen frameworks, the 3D open-framework chalcogenides have a much higher structural polarability owning to the larger sizes and more delocalized orbitals of chalcogen atoms than oxygen. These features allow us to obtain a semiconducting open-framework by constructing 3D chalcogenide structures,[7] which can have potential applications in thermal, electronic, optical, and catalytic fields. Therefore, considerable efforts have been devoted to developing new 3D open-framework chalcogenides. Like the oxygen based zeolites, most of the 3D open-framework chalcogenides are constructed by tetrahedra based on group 13 and group 14 elements,[7,18−24] even though the tetrahedral sites can be replaced by supertetrahedra.[25−32]

Received: February 11, 2015
Published: May 8, 2015

DOI: 10.1021/acs.inorgchem.5b00317
Inorg. Chem. 2015, 54, 5301−5308

Table 1. Crystallographic Data and Details of the Structure Refinement for $Na_4Cu_{32}Sn_{12}S_{48}\cdot 4H_2O$ and $K_{11}Cu_{32}Sn_{12}S_{48}\cdot 4H_2O$

formula	$Na_4Cu_{32}Sn_{12}S_{48}\cdot 4H_2O$	$K_{11}Cu_{32}Sn_{12}S_{48}\cdot 4H_2O$
formula wt	5161.32	5499.25
space group	$Fm\bar{3}c$	$Fm\bar{3}c$
unit cell (Å)	a = 17.921(2)	a = 18.0559(6)
vol (Å^3)	5755.5(12)	5886.5(3)
Z	2	2
calcd density	2.978 g/cm^3	3.104 g/cm^3
index ranges	$-24 \le h \le 23$, $-13 \le k \le 23$, $-23 \le l \le 11$	$-23 \le h \le 13$, $-23 \le k \le 4$, $-23 \le l \le 15$
reflns collected	2818	1106
unique reflns	303	306
goodness-of-fit on F^2	1.310	1.256
R [$I > 2\sigma(I)$]	0.0435	0.0539
wR2 [$I > 2\sigma(I)$]	0.1005	0.1591
R (all)	0.0524	0.0688
wR2 (all)	0.1049	0.1683

The group 11 metal ions (Cu^+) can adopt a variety of coordination modes with chalcogen atoms ranging from linear[33] to trigonal[34] and tetrahedral geometries.[34] Therefore, the building blocks formed by group 11 metal ions (Cu^+) with chaolcogens exhibit various forms, for instance large clusters (0D),[33] complex chains (1D),[35] and layers (2D).[34] However, few 3D open-framework chalcogenides are built up by group 11 metal ions. From the point view of electronic band structure, Cu_2S has a narrow band gap with the d-orbitals of Cu^+ and the p-orbitals of S^{2-} anions at the valence band maximum (VBM).[36] Meanwhile, the conduction band minimum (CBM) mainly consists of empty s-orbitals of the Cu^+ ion. The band structure of Cu/S-based compounds can easily be modulated by partially replacing the Cu^+ ions with Cu^{2+} ions, which downshifts the VBM and generates unfilled Cu 3d orbitals. The most intriguing result for this band modulation is the transparent conductive phenomena in Cu/S-based materials with p-type electrical conduction.[4] As main group metal chalcogenides, SnS_2 is an indirect band semiconductor, with the gap energy of 2.1 eV.[37] The CBM are also mainly the empty s-orbital of Sn^{4+} ions which is hybridized with the S 3p orbitals. Remarkably, the Cu 3d and 4s orbitals are always orthogonal to the Sn 5s orbitals, implying very weak interaction between them. Our previous work showed that if two orbitals from different building blocks are both in the CBM but have weak overlap, they can feature multiband character in the electronic structure of the combined compounds.[1] Therefore, we can combine Cu/S and Sn/S structural motifs to produce a multiband compound. In addition, the Sn/S structural motif is regularly used in building up 3D open-framework chalcogenides. Therefore, we can integrate the advantages of 3D open-framework chalcogenides together with multiband properties in a single compound if we can construct the Cu/Sn/S 3D open frameworks. In this way, we can obtain a multifunctional material for special applications.

Combining the structural and functional features of simple Cu/S- and Sn/S-based compounds, we have made efforts to incorporate Cu/S and Sn/S building blocks in a multicomponent compound with 3D open-framework topologies. Herein, we report two new quaternary 3D open-framework sulfides $Na_4Cu_{32}Sn_{12}S_{48}\cdot 4H_2O$ and $K_{11}Cu_{32}Sn_{12}S_{48}\cdot 4H_2O$ consisting of copper rich $[Cu_8Sn_6S_{24}]^{z-}$ clusters. The compounds feature a 3D porous structure, which are filled with charge-balancing cations (Na^+ or K^+). The optical and photoelectronic related properties of the compounds were characterized. The compounds show typical multiband properties. The electrical conductivity of the two compounds was also measured, showing that the $Na_4Cu_{32}Sn_{12}S_{48}\cdot 4H_2O$ is a good ionic conductor. Theoretical calculations were also performed to understand the electronic structure and the related properties.

EXPERIMENTAL SECTION

Reagent. All the starting materials were obtained from Sinopharm Chemical Reagent Beijing Co., Ltd.: (i) sodium hydroxide, AR, 96%; (ii) anhydrous potassium carbonate, AR, 99%; (iii) copper powder, 99.7%; (iv) tin disulfide, 99.5%; (v) thiourea, AR, 99%; (vi) sulfur powder, sublimed, 99.5%. All the reagents were kept in a drybox. No further purifications were performed before use.

Synthesis of $Na_4Cu_{32}Sn_{12}S_{48}\cdot 4H_2O$. Starting materials of NaOH (10.0 g), Cu powder (0.318 g, 5.0 mmol), SnS_2 powder (0.914 g, 5.0 mmol), and thiourea powder (7.61 g, 0.1 mol) were weighed and ground uniformly, and placed into a Teflon-lined steel autoclave. The Teflon-lined steel autoclave was tightly sealed and heated at 473 K for 3 days. Then the autoclave was pulled out of a hot oven and allowed to cool to ambient temperature. After cooling to room temperature, the product was ultrasonically cleaned using distilled water until the black crystals were separated. Then the crystals were washed using distilled water for several times in open air and dried by acetone. The final yield is about 48.8% based on the 5 mmol of Cu. The presence of Na, Cu, Sn, and S was confirmed by semiquantitative energy dispersive X-ray analysis on a Hitachi S-4800 scanning electron microscope (SEM). Ten different crystals were chosen, and their average atomic ratio of Na/Cu/Sn/S was 4.5(0.5)/35.6(0.9)/14.1(0.3)/46.8(1.2). The SEM image and element identification results of $Na_4Cu_{32}Sn_{12}S_{48}\cdot 4H_2O$ are included in Figure S1a,c in the Supporting Information. The concentration of each metal ion in the crystals was determined by inductively coupled plasma atomic emission spectrum (ICP-AES). The results are shown in Table S1 in the Supporting Information.

Synthesis of $K_{11}Cu_{32}Sn_{12}S_{48}\cdot 4H_2O$. Starting materials of K_2CO_3 (17.3 g), Cu powder (0.318 g, 5.0 mmol), SnS_2 powder (0.914 g, 5.0 mmol), and S powder (0.8 g, 25 mmol) were weighed and ground uniformly, and placed into a Teflon-lined steel autoclave. Then 10 mL of distilled water was added. The Teflon-lined steel autoclave was tightly sealed and heated at 473 K for 3 days. Then the autoclave was pulled out of a hot oven and allowed to cool to ambient temperature. After cooling to room temperature, the product was treated in the same way as for $Na_4Cu_{32}Sn_{12}S_{48}\cdot 4H_2O$. Black crystals were obtained with final yield about 70.2% based on the 5 mmol of Cu. The presence of K, Cu, Sn, and S was confirmed by semiquantitative energy dispersive X-ray analysis on a Hitachi S-4800 SEM. Ten different crystals were chosen, and their average atomic ratio of K/Cu/Sn/S was 10.5(0.8)/31.7(0.4)/12.2(0.6)/45.6(1.1). The SEM image and element identification results of $K_{11}Cu_{32}Sn_{12}S_{48}\cdot 4H_2O$ are included in Figure S1b,d in the Supporting Information. The concentration of

DOI: 10.1021/acs.inorgchem.5b00317
Inorg. Chem. 2015, 54, 5301−5308

each metal ion in the crystals was determined by ICP-AES. The results are shown in Table S1 in Supporting Information.

Single Crystal X-ray Crystallography. Single crystals suitable for X-ray diffraction were chosen from the as-prepared samples. Data collection was performed on an Agilent Super Nova diffractometer equipped with mirror-monochromated Mo Kα radiation. The structures of the two compounds were solved by direct methods and refined by full-matrix least-squares on F^2 using the SHELXTL program package.[38] Multiscan absorption corrections were performed. The crystal data and refinement details are summarized in Table 1.

Powder X-ray Diffraction (PXRD). The synthesized crystal samples were ground and used to verify the phase purity on a Rigaku X-ray diffractometer (Cu Kα). Simulated patterns were generated using the CrystalMaker program and the CIF of the refined structure.

UV−Vis Light Spectroscopy. Optical diffuse-reflectance measurements were carried out using a UV-4100 spectrophotometer operating from 2000 to 300 nm at room temperature. The $BaSO_4$ powder was used as a 100% reflectance standard. The powder samples were spread on a compacted base of $BaSO_4$ powder. The generated reflectance-versus-wavelength data were used to measure the band gap of the material. The reflectance data was converted to absorbance data using the Kubelka−Munk equation.[39]

Fourier Transform Infrared Spectroscopy. Before use, the two compounds were ground into fine powders and dried in a vacuum oven at 60 °C overnight. Afterward, the fine powders were grounded with KBr and pressed into thin slices. FT-IR spectra are measurements were carried out using Magna-IR 750 operating from 4000 to 1500 cm^{-1} at room temperature.

Thermogravimetric Measurements. The crystal samples are dried overnight in a vacuum oven at 60 °C to remove the absorbed water. The thermogravimetric measurements were performed on a Q600SDT thermogravimetric analyzer. The operating temperature ranges from 20 to 800 °C with the heating rate of 10 °C/min. Nitrogen, with flow rate of 100 mL/min, was used as the protective gas.

Magnetic Property Measurements. The magnetic properties of the as-prepared compounds were studied using a superconducting quantum interference device magnetometer (Quantum design, MPMS). The dc susceptibility measurements, under both zero-field-cooling (ZFC) and field-cooling (FC) conditions, were performed in a 1000 Oe magnetic field for temperatures ranging from 2 to 300 K.

Dye Absorption and Photocatalysis. In all dye absorption and catalytic experiments, the temperature was kept at room temperature by using a circulating water jack to prevent any thermal degradation effect. The initial 10 mg/L methylene blue (MB) solution was used. The powder concentration in the neutral MB aqueous solution was 0.1 g/100 mL. The mixture was first magnetically stirred in a dark room. During the absorption process, about 5 mL of suspension was continually taken from the reaction cell at given time intervals for subsequent MB concentration analysis after centrifuging. When reaching the adsorption−desorption equilibrium of MB on catalysts, the visible light (cutoff wavelengths <420 nm) illumination was conducted for the suspension. During irradiation, about 5 mL of suspension was continually taken from the reaction cell at given time intervals for subsequent MB concentration analysis after centrifuging.

Ionic Conductivity Measurements. The ionic conductivity of the two compounds was measured by ac impedance methods. The measurement frequency ranges from 0.01 to 1000000 Hz using an electrochemical workstation. The as-prepared crystals were ground and press into pellets at the pressure of 20 MPa. The indium metal was used as contacting electrodes.

Electronic Structure Calculations. The first-principles computations based on the density-functional theory (DFT) were performed using the Vienna ab initio simulation package (VASP). The Perdew−Burke−Ernzerhof (PBE) version of the generalized gradient approximation (GGA)[40] was used to describe the exchange correlation functional, and the projector augmented wave (PAW)[41] method was used in the present work. Here, the cutoff energy of plane wave was chosen at 350 eV. For the structure optimizations, 6 × 6 × 6 Monkhorst−Pack grids were used for the primitive cell and 4 × 4 × 4 k-points for the conventional cell, respectively. The relaxation of geometry optimization was performed until the total energy changes within 10^{-6} eV/atom and the Hellmann−Feynman force on all atomic sites was less than 0.01 eV/Å.

RESULTS AND DISCUSSION

Synthesis and Crystal Structure Description. Low temperature synthesis including solvothermal method and reactive flux method can produce mild reaction conditions, which is beneficial to the synthesis of metastable phases.[42−44] Thiourea can slowly release S at a relatively higher temperature than its melting point (182 °C), making it a good candidate of sulfur sources.[44] Similar to the A_2Q/Q melts, thiourea can be used as the reactive flux for low temperature synthesis of sulfides. With the assistance of NaOH as the mineralizer and thiourea as reactive flux, we synthesized the $Na_4Cu_{32}Sn_{12}S_{48}\cdot 4H_2O$ single crystals with cubic shape (Figure S1a in the Supporting Information). Instead, the cubic $K_{11}Cu_{32}Sn_{12}S_{48}\cdot 4H_2O$ crystals (Figure S1b in the Supporting Information) are synthesized via hydrothermal method.

Two $A_{16-x}Cu_{32}Sn_{12}S_{48}\cdot 4H_2O$ compounds ($Na_4Cu_{32}Sn_{12}S_{48}\cdot 4H_2O$ and $K_{11}Cu_{32}Sn_{12}S_{48}\cdot 4H_2O$) are crystallized in the cubic system of space group $Fm\bar{3}c$ (Figure 1a). Both the structures

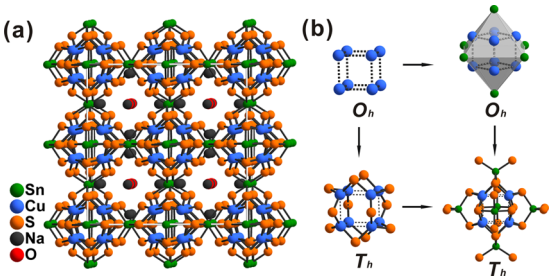

Figure 1. (a) Crystal structure of $Na_4Cu_{32}Sn_{12}S_{48}\cdot 4H_2O$ viewed along [001]. (b) The construction of the $[Cu_8Sn_6S_{24}]^{z-}$ cluster.

feature isotropic 3D open-framework $[Cu_{32}Sn_{12}S_{48}]^{n-}$ (n = 4 for $Na_4Cu_{32}Sn_{12}S_{48}\cdot 4H_2O$; n = 11 for $K_{11}Cu_{32}Sn_{12}S_{48}\cdot 4H_2O$), which are isostructural to the 3D open-framework $[Cu_{32}Ge_{12}S_{48}]^{16-}$ in $K_4Cu_8Ge_3S_{12}$.[45] The crystal structure contains one unique A site (A = Na, K), one unique Cu site, one unique Sn site, one unique S site, and one unique O site at the Wyckoff positions of 48f, 64g, 24c, 96i, and 48f, respectively.

The $[Cu_8Sn_6S_{24}]^{z-}$ clusters (Figure 1b), serving as the building blocks, connect with each other via $[SnS_4]^{4-}$ tetrahedra to form a 3D open framework. The cluster consists of eight $[CuS_3]$ triangles and six $[SnS_4]$ tetrahedra. The cubes of eight Cu atoms (Figure 1b) are coordinated to 12 S atoms to form $[Cu_8S_{12}]$ clusters with the T_h symmetry. The 12 S atoms in the $[Cu_8S_{12}]$ cluster are located at the vertex of a Platonic icosahedron, in which the Cu_8 Platonic cubes are encapsulated. The six distorted $[SnS_4]$ tetrahedra cap the Platonic icosahedron forming the $[Cu_8Sn_6S_{24}]^{z-}$ cluster of the T_h symmetry. It is worthy to note that the six Sn atoms, which cap the six faces of the $[Cu_8]$ cube, form a Platonic octahedron (Figure 1b). Therefore, the 3D open framework formed by the $[Cu_8Sn_6S_{24}]^{z-}$ clusters via corner sharing. This copper rich cluster is also present in $(H_2en)_2Cu_8Sn_3S_{12}$.[15] Note that our 3D open framework is not the same as that of $(H_2en)_2Cu_8Sn_3S_{12}$. Another similar connection appears in $[M(NH_3)_6]Cu_8Sb_3S_{13}$ (M = Mn, Fe, Ni), $(H_2en)_{1.5}[Cu_8(\mu_8\text{-}Se)(AsSe_4)_{2/6}]$,

DOI: 10.1021/acs.inorgchem.5b00317
Inorg. Chem. 2015, 54, 5301−5308

$(H_2dap)_{1.5}[Cu_8(\mu_8\text{-}Se)(AsSe_4)_{2/6}]$, and $Na_2(H_2dap)_{0.5}[Cu_8(\mu_8\text{-}Se)(AsSe_4)_{2/6}]$ in which copper sulfide cores are linked together by group 15 elements (As or Sb).[46] The Cu−S distance is 2.268(2) Å and 2.253(3) Å in $Na_4Cu_{32}Sn_{12}S_{48}\cdot 4H_2O$ and $K_{11}Cu_{32}Sn_{12}S_{48}\cdot 4H_2O$, respectively. Remarkably, the S−Cu−S angle is 119.15(2)° in $Na_4Cu_{32}Sn_{12}S_{48}\cdot 4H_2O$ and 119.34(2)° in $K_{11}Cu_{32}Sn_{12}S_{48}\cdot 4H_2O$, indicating that the $[CuS_3]$ base is not a regular triangle in both compounds. The Sn−S distance is 2.408(2) Å in $Na_4Cu_{32}Sn_{12}S_{48}\cdot 4H_2O$ and 2.404(5) Å in $K_{11}Cu_{32}Sn_{12}S_{48}\cdot 4H_2O$, respectively. These distances are comparable to those in the reported structure (2.401 Å for the Sn−S average length in $Na_4Sn_3S_8$). The connection parts of two nearest $[Cu_8Sn_6S_{24}]^{z-}$ clusters, namely, the $[SnS_4]^{4-}$ tetrahedra, suffer a slightly squashed distortion along the direction pointing from one $[Cu_8Sn_6S_{24}]^{z-}$ cluster to another in both compounds with the biggest S−Sn−S angles of 113.2(1)° and 110.42(3)° in $Na_4Cu_{32}Sn_{12}S_{48}\cdot 4H_2O$ and $K_{11}Cu_{32}Sn_{12}S_{48}\cdot 4H_2O$, respectively.

The Na−O and K−O distances are 3.41(4) Å and 3.15(2) Å, which are longer than that in alkali metal oxide (2.383 Å in Na_2O and 2.740 Å in K_2O) and hydroxides (2.375 Å in NaOH and 2.842 Å in KOH). Due to theses long distances between oxygen and alkali metal ions, we propose that the oxygen belongs to free water instead of O^{2-} or OH^-. FT-IR spectra were obtained, and thermogravimetric analyses were conducted. The FT-IR spectra of the two compounds (Figure S2 in the Supporting Information) show intense absorption peaks around 3300 cm^{-1}, which are attributed to the O−H stretching in the compounds. Besides, both compounds show weight loss at low temperature (~150 °C) in the corresponding thermogravimetric curves (Figure S3 in the Supporting Information), which further proved the presence of water in the two compounds.

Eight $[Cu_8Sn_6S_{24}]^{z-}$ clusters connect with each other via $[SnS_4]$ tetrahedra, leaving a cage between the clusters occupied by the alkali metal ions and free water (Figure 2a, the space

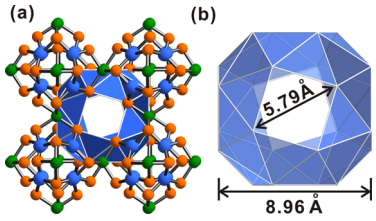

Figure 2. (a, b) Schematic diagrams of the cages formed by eight $[Cu_8Sn_6S_{24}]^{z-}$ clusters.

surrounded by the blue planes). The cage, as the building block of the 3D porous structure, connects with six equal cages via the uncapped square planes. The biggest diameter of the cage is about 8.96 Å (Figure 2b). Remarkably, alkali metal ions do not fully occupy the 48f site in the cages. The final atomic ratios of the two compounds from the inductively coupled plasma atomic emission spectrum (ICP-AES) results (Table S1 in the Supporting Information) can further prove the existence of the A-site vacancies. Due to these vacancies, the alkali metal ions are able to migrate between the cages. The diagonal of the uncapped square planes (as a gate of the cage) is 5.79 Å, about as twice as large as the average Na−S distance in common NaS-based compounds (2.835 Å in Na_2S, 2.856 Å in $Na_4Cu_2S_3$, 2.932 Å in $Na_4Sn_3S_8$, and 2.93, Å in Na_3PS_4[47,48]). This indicates that the Na^+ ions can easily migrate through the gate and travel in the 3D porous structure.

The oxidation states of A, Cu, Sn, and S in $A_{16}Cu_{32}Sn_{12}S_{48}\cdot 4H_2O$ are +1, +1, +4, and −2, respectively. The partial occupation of the A site in $A_{16-x}Cu_{32}Sn_{12}S_{48}\cdot 4H_2O$ ($Na_4Cu_{32}Sn_{12}S_{48}\cdot 4H_2O$, $K_{11}Cu_{32}Sn_{12}S_{48}\cdot 4H_2O$) requires the presence of Cu^{2+} to balance the charge. In $Na_4Cu_{32}Sn_{12}S_{48}\cdot 4H_2O$, the occupancy of the A site is 25%, consequently 37.5% of Cu is in the +2 state; in $K_{11}Cu_{32}Sn_{12}S_{48}\cdot 4H_2O$, the occupancy of the A site is 69%, and 15.6% of Cu is in +2 state. The magnetic property measurements are used to further prove the presence of Cu^{2+} ions in the two compounds (Figure S4 in the Supporting Information). Paramagnetic properties of these two compounds demonstrate the Cu^{2+} ions existing in $A_{16-x}Cu_{32}Sn_{12}S_{48}\cdot 4H_2O$ due to the only magnetic moment from Cu^{2+}. The $M-T$ curves can be fitted by the Curie−Weiss law, while the numbers of spins (per $[Cu_8Sn_6S_{24}]^{z-}$ cluster) are calculated with the value of 3.1 for $Na_4Cu_{32}Sn_{12}S_{48}\cdot 4H_2O$ and 1.2 for $K_{11}Cu_{32}Sn_{12}S_{48}\cdot 4H_2O$. Therefore, 38.3% of Cu is in the +2 state in $Na_4Cu_{32}Sn_{12}S_{48}\cdot 4H_2O$ and 15% of Cu is in the +2 state in $K_{11}Cu_{32}Sn_{12}S_{48}\cdot 4H_2O$, which is consistent with the number calculated from charge balance.

PXRD and Optical Absorption. The pure phases of the two compounds were confirmed by PXRD. As illustrated in Figure 3, the pattern of the powder sample matched well with

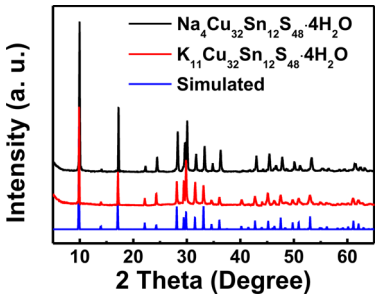

Figure 3. Powder X-ray diffraction patterns of $Na_4Cu_{32}Sn_{12}S_{48}\cdot 4H_2O$ and $K_{11}Cu_{32}Sn_{12}S_{48}\cdot 4H_2O$. The simulated pattern of $K_{11}Cu_{32}Sn_{12}S_{48}\cdot 4H_2O$ is obtained by *CrystalMaker* programs.

that simulated from $K_{11}Cu_{32}Sn_{12}S_{48}\cdot 4H_2O$ single crystal data using the *CrystalMaker* program. No extra peaks were observed. Furthermore, the diffraction peaks of $Na_4Cu_{32}Sn_{12}S_{48}\cdot 4H_2O$ had evidently moved in the low-angle region compared to the peaks of $K_{11}Cu_{32}Sn_{12}S_{48}\cdot 4H_2O$, indicating the decrease of the lattice constant.

The optical properties of the two compounds were investigated by UV−visible diffuse reflectance spectrum (UV−vis), as depicted in Figure 4a. Both compounds show intense absorbance of ultraviolet and visible light. This indicates that $Na_4Cu_{32}Sn_{12}S_{48}\cdot 4H_2O$ and $K_{11}Cu_{32}Sn_{12}S_{48}\cdot 4H_2O$ are relatively narrow band gap semiconductors. In addition to the full solar spectrum absorption, there are an absorption peak and an absorption edge in the spectra. The absorption peak is located at 770 nm (1.61 eV) for $Na_4Cu_{32}Sn_{12}S_{48}\cdot 4H_2O$ and 820 nm (1.52 eV) for $K_{11}Cu_{32}Sn_{12}S_{48}\cdot 4H_2O$, respectively. These additional absorption peaks indicate that the two compounds have multiband absorptions matching the multiband features in the electronic structure. The band gap of $Na_4Cu_{32}Sn_{12}S_{48}\cdot 4H_2O$ and $K_{11}Cu_{32}Sn_{12}S_{48}\cdot 4H_2O$ was estimated from the absorption spectrum by using an extrapolation method, as illustrated in Figure S5 in the Supporting Information. The main absorption

DOI: 10.1021/acs.inorgchem.5b00317
Inorg. Chem. 2015, 54, 5301−5308

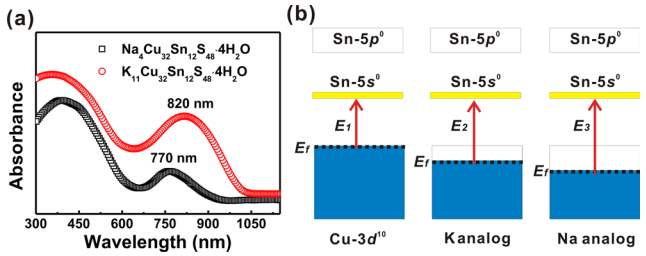

Figure 4. (a) Solid-state UV−visible diffuse reflectance spectra of $Na_4Cu_{32}Sn_{12}S_{48}\cdot 4H_2O$ and $K_{11}Cu_{32}Sn_{12}S_{48}\cdot 4H_2O$. (b) Schematic band structure of Cu/Sn/S based materials with different concentration of Cu^{2+} in the compounds.

edge of $Na_4Cu_{32}Sn_{12}S_{48}\cdot 4H_2O$ is 621 nm (2.0 eV), while a red shift occurs for $K_{11}Cu_{32}Sn_{12}S_{48}\cdot 4H_2O$ with the main absorption edge located around 643 nm (1.9 eV). It is known that the Sn 5s states are important for the multiband properties of the Cu/Sn/S system.[49] Therefore, we propose an electronic structure model as shown in Figure 4b. The transition from the VBM to the Sn 5s states, which is located in the middle of the Cu-3d and Sn-5p states, results in the multiband absorption. The red shifts of both absorption peak and edge of $K_{11}Cu_{32}Sn_{12}S_{48}\cdot 4H_2O$ are understandable. Increase of the Cu $3d^9$ electronic states in $Na_4Cu_{32}Sn_{12}S_{48}\cdot 4H_2O$ (x = 12 in $A_{16-x}Cu_{32}Sn_{12}S_{48}\cdot 4H_2O$ and 37.5% Cu^{2+}) will leave more unfilled Cu 3d states, compared with $K_{11}Cu_{32}Sn_{12}S_{48}\cdot 4H_2O$ (x = 5 in $A_{16-x}Cu_{32}Sn_{12}S_{48}\cdot 4H_2O$ and 15.6% Cu^{2+}), as shown in Figure 4b.

Electrical Conductivity. Due to the alkali metal ions located in the open 3D framework and the partial occupation which led to the vacancies in the porous structure, the alkali metal ions may migrate in the structure. The ac impedance spectrum at room temperature of a $Na_4Cu_{32}Sn_{12}S_{48}\cdot 4H_2O$ disk, measured with Ag electrodes, is plotted in Figure 5a. Two semicircular arcs are present, which is attributed to bulk behavior (the first arc) and grain boundary behavior (the second arc). These arcs are common characteristics of the Nyquist plot of ion-conducting polycrystalline ceramics.[47,50−53] The spike in the low frequency region shows the blocking nature of the electrode,[51,54] indicating the presence of ionic conductivity in the $Na_4Cu_{32}Sn_{12}S_{48}\cdot 4H_2O$ disk. The conductivity can be calculated with the equation $\sigma = L/(RS)$, where the L refers to the thickness of the $Na_4Cu_{32}Sn_{12}S_{48}\cdot 4H_2O$ disk, S is the area in contact with the electrodes, and R is the real impedance measured from the location of the local minima between the high and low frequency arc on the real axis of the Nyquist plot. The final total electrical conductivity is 3.4×10^{-5} S/cm at room temperature, comparable to that of the $Na_2Se-Ga_2Se_3-GeSe_2$ glass ceramic.[51] The Arrhenius plot of the total and bulk conductivity of $Na_4Cu_{32}Sn_{12}S_{48}\cdot 4H_2O$ disk is shown in Figure 5b. The activation energy E_a is obtained from the equation

$$\sigma_T = \sigma_0 \exp(-E_a/k_BT) \quad (1)$$

where σ_T is the total conductivity, σ_0 is the pre-exponential coefficient, T is the absolute temperature, k_B is the Boltzmann constant, and E_a is the activation energy. The activation energy of $Na_4Cu_{32}Sn_{12}S_{48}\cdot 4H_2O$ is 0.25 eV for the total conductivity. The dc-polarization and $I-V$ curves of the $Na_4Cu_{32}Sn_{12}S_{48}\cdot 4H_2O$ disk with Ag electrodes are shown in Figures 5c and 5d, respectively. The $I-V$ curve confirms the ohmic behavior of the cell in the voltage range from −10 to 10 mV. In this ohmic regime, the cell undergoes polarization under a constant bias due to the accumulation of Na^+ at the negative electrode. The initial current is 3.02 μA at 10 mV and decreases to 1.48 μA after 10 min. After that, the current decreases much more slowly, which can be assumed to be in the steady state. Then the transference number for Na^+ conductivity of the $Na_4Cu_{32}Sn_{12}S_{48}\cdot 4H_2O$ disk is higher than 51%, implying that the ionic migration is dominant in the total conductivity.

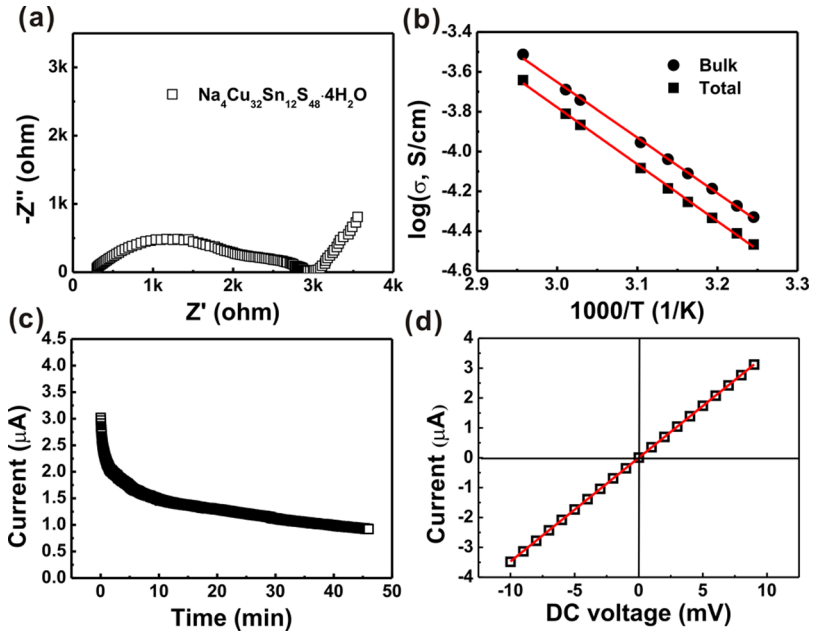

Figure 5. (a) Nyquist plot of the as-prepared $Na_4Cu_{32}Sn_{12}S_{48}\cdot 4H_2O$ disk. (b) Arrhenius plot of the total and bulk conductivity of $Na_4Cu_{32}Sn_{12}S_{48}\cdot 4H_2O$ disk. (c) Dc-polarization curve of the $Na_4Cu_{32}Sn_{12}S_{48}\cdot 4H_2O$ disk with Ag electrodes measured at room temperature. (d) $I-V$ curve of the $Na_4Cu_{32}Sn_{12}S_{48}\cdot 4H_2O$ disk with Ag electrodes in the voltage range from −10 to 10 mV.

DOI: 10.1021/acs.inorgchem.5b00317
Inorg. Chem. 2015, 54, 5301−5308

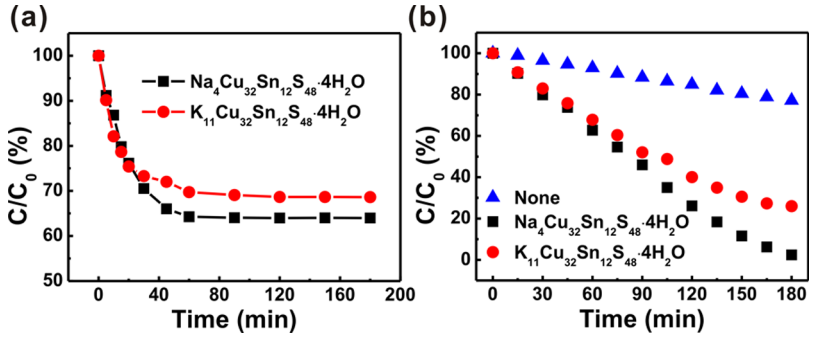

Figure 6. (a) Concentration evolution during the dark room absorption process of $Na_4Cu_{32}Sn_{12}S_{48}\cdot 4H_2O$ and $K_{11}Cu_{32}Sn_{12}S_{48}\cdot 4H_2O$ crystals. (b) Concentration evolution during the visible-light photocatalytic process of $Na_4Cu_{32}Sn_{12}S_{48}\cdot 4H_2O$ and $K_{11}Cu_{32}Sn_{12}S_{48}\cdot 4H_2O$ crystals.

Even though the $K_{11}Cu_{32}Sn_{12}S_{48}\cdot 4H_2O$ has a similar structure to $Na_4Cu_{32}Sn_{12}S_{48}\cdot 4H_2O$, and there are also vacancies in the 3D porous structure, the $K_{11}Cu_{32}Sn_{12}S_{48}\cdot 4H_2O$ disk does not show any dc-polarization character (Figure S6 in the Supporting Information). The Nyquist plot shows neither semicircular arc in the full frequency range. This might be due to the larger ionic radius of K^+ than Na^+ which leads to the difficulty of K^+ ions going through the gate of the cages formed by eight $[Cu_8Sn_6S_{24}]^{z-}$ clusters.

Dye Absorption and Visible-Light Photocatalysis. The multiband absorption feature can efficiently utilize the sunlight and generate many more electron−hole pairs. This implies that the two compounds may catalyze the decomposition reaction of organic dyes. The decomposition reaction of methylene blue (MB) is used as a probe to evaluate the photocatalytic properties of the two compounds. First, the absorption processes of MB are established in the dark, and the plot of absorption percentage vs time is shown in Figure 6a. Obviously, both compounds reveal good absorption for MB. At about 60 min, both compounds reach the absorption equilibrium with the absorption percentage of 35% for $Na_4Cu_{32}Sn_{12}S_{48}\cdot 4H_2O$ and 30% for $K_{11}Cu_{32}Sn_{12}S_{48}\cdot 4H_2O$. The slightly higher absorption amount of $Na_4Cu_{32}Sn_{12}S_{48}\cdot 4H_2O$ than $K_{11}Cu_{32}Sn_{12}S_{48}\cdot 4H_2O$ might due to the large amount of vacancies at the 48i site of $Na_4Cu_{32}Sn_{12}S_{48}\cdot 4H_2O$ than $K_{11}Cu_{32}Sn_{12}S_{48}\cdot 4H_2O$. The photocatalytic process begins when the visible light is on, and the concentration evolution of MB is demonstrated in Figure 6b. Remarkably, the acceleration of degradation rate over both compounds was observed. After the 3 h irradiation, almost 70% of MB was degraded when catalyzed by $K_{11}Cu_{32}Sn_{12}S_{48}\cdot 4H_2O$ crystals, while the $Na_4Cu_{32}Sn_{12}S_{48}\cdot 4H_2O$ crystals can degrade almost 100% of MB within 3 h. The good catalytic properties of both compounds are attributed to the electron and hole generation under the visible-light irradiation. The optical results have shown that the two compounds have good absorption properties for the full spectrum of sunlight, accompanying the absorption peaks at the red light region. This explains why the two new 3D open frameworks have visible-light driven photocatalytic activities.

Electronic Band Structure. The first principle calculations were performed to understand the electronic structure of the two compounds. The two compounds have similar electronic structure because they have the same structure and the lack of contributions to the valence band maximum (VBM) and conduction band minimum (CBM) of the alkali metal ions. Therefore, only the electronic structure of the $Na_4Cu_{32}Sn_{12}S_{48}\cdot 4H_2O$ compound is discussed here. The band structure and total density of states are shown in Figure 7a,b. The band structure indicates that both VBM and CBM are at Γ(0,0,0).

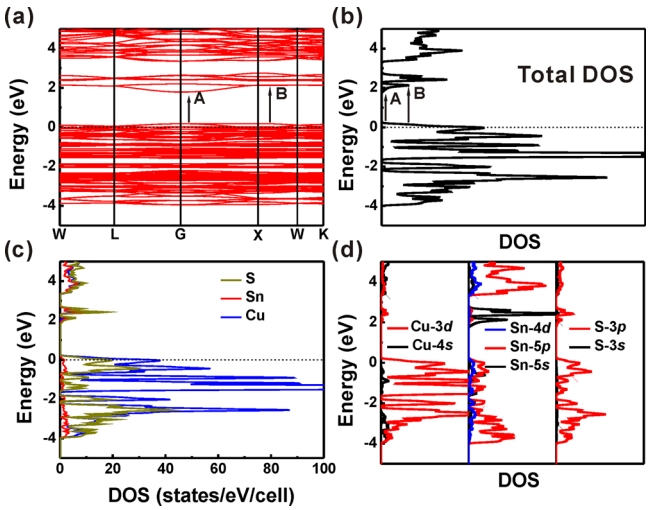

Figure 7. (a, b) Electronic band structure and total density of states of the $Na_4Cu_{32}Sn_{12}S_{48}\cdot 4H_2O$ compound. (c,d) Partial density of states of the $Na_4Cu_{32}Sn_{12}S_{48}\cdot 4H_2O$ compound.

Furthermore, the band structure features a multiband structure with intermediate band sets located in the energy range of 1.5 to 3 eV in the CB. The electron transitions occur from VBM to band B (Figure S7 in the Supporting Information), with energy about 2 eV that matches well with the main band gap from the UV−vis light spectrum. There is an additional experimental optical absorption peak (1.6 eV) for $Na_4Cu_{32}Sn_{12}S_{48}\cdot 4H_2O$, which can be attributed to the transition from VBM to band A in the CB (Figure S7 in the Supporting Information).

The experimental optical absorption edges can be explained from the analyses of the total and partial density of states (DOS) in Figure 7b−d. The Cu-3d states play a very important role in constructing the valence band. There is up to 92% Cu-3d states located in the energy regime of −4 to 0 eV. The CBM is dominated by the Sn-5s states. The Sn-5s states, mainly located in the range of 1.5−3 eV (Figures 7c,d), act as intermediate bands. The main absorption edge (~2 eV), like the additional absorption peak (~1.6 eV), are from the transitions of Cu-3d-S-3p → Sn-5s. Overall, the Sn-5s states play a very important role on the multiabsorption edges of both compounds.

It is worthy to note that the Fermi level of $Na_4Cu_{32}Sn_{12}S_{48}\cdot 4H_2O$ is lower than that of $K_{11}Cu_{32}Sn_{12}S_{48}\cdot 4H_2O$ (Figure S8 in

DOI: 10.1021/acs.inorgchem.5b00317
Inorg. Chem. 2015, 54, 5301−5308

the Supporting Information), which leads to the larger band gap of $Na_4Cu_{32}Sn_{12}S_{48}\cdot 4H_2O$ than that of $K_{11}Cu_{32}Sn_{12}S_{48}\cdot 4H_2O$.

CONCLUSION

In summary, we have successfully synthesized, via flux and hydrothermal method, two new compounds $Na_4Cu_{32}Sn_{12}S_{48}\cdot 4H_2O$ and $K_{11}Cu_{32}Sn_{12}S_{48}\cdot 4H_2O$, which are based on the $[Cu_8Sn_6S_{24}]^{z-}$ (z = 13 for $Na_4Cu_{32}Sn_{12}S_{48}\cdot 4H_2O$ and 14.75 for $K_{11}Cu_{32}Sn_{12}S_{48}\cdot 4H_2O$) clusters. For the first time, we successfully integrated the advantage of 3D open frameworks together with the multiband properties in a single phase material. The structure features an alkali metal ion filled 3D open framework with the $[Cu_8Sn_6S_{24}]^{z-}$ clusters (T_h symmetry) serving as building blocks. The combination of the CuS motif and SnS motif, which usually possess nonoverlap of orbitals, resulted in a much more complex absorption character. The main optical absorption edges around 2.0 eV for $Na_4Cu_{32}Sn_{12}S_{48}\cdot 4H_2O$ and 1.9 eV for $K_{11}Cu_{32}Sn_{12}S_{48}\cdot 4H_2O$, together with the additional absorption peaks around 1.61 eV for $Na_4Cu_{32}Sn_{12}S_{48}\cdot 4H_2O$ and 1.52 eV for $K_{11}Cu_{32}Sn_{12}S_{48}\cdot 4H_2O$, are present. The first principle calculation results reveal that the Sn-5s orbitals, which are located in the middle of the Cu-3d-S-3p → Sn-5p gap, play an important role in constructing the CBM. The red shift of the band gap energy of $K_{11}Cu_{32}Sn_{12}S_{48}\cdot 4H_2O$ is due to the higher Fermi level than that of $Na_4Cu_{32}Sn_{12}S_{48}\cdot 4H_2O$. In addition, the two optical absorption peaks are attributed to the two transitions of Cu-3d-S-3p → Sn-5s. The $Na_4Cu_{32}Sn_{12}S_{48}\cdot 4H_2O$ shows ionic conduction nature in the 3D open-framework structure with the total conductivity of 3.4×10^{-5} S/cm at room temperature.

ASSOCIATED CONTENT

Supporting Information

SEM, EDX, FT-IR, TGA, and ICP-AES results. Magnetic measurements and results. The plot of $F^{1/2}(R)$ against photon energy, dc-polarization curve of the $K_{11}Cu_{32}Sn_{12}S_{48}\cdot 4H_2O$ disk, and total density of states of the $Na_4Cu_{32}Sn_{12}S_{48}\cdot 4H_2O$ and $K_{11}Cu_{32}Sn_{12}S_{48}\cdot 4H_2O$. Crystallographic data in CIF format. The Supporting Information is available free of charge on the ACS Publications website at DOI: 10.1021/acs.inorgchem.5b00317.

AUTHOR INFORMATION

Corresponding Author

*E-mail: huangfq@pku.edu.cn.

Author Contributions

‡X.Z., Q.W., and Z.M. contributed equally.

Notes

The authors declare no competing financial interest.

ACKNOWLEDGMENTS

Financial support from 863 Program of China (Grant 2011AA050505), the NSF of China (Grants 91122034, 51125006, 51121064, 61376056), the CAS/SAFEA International Partnership Program for Creative Research Teams, "Strategic Priority Research Program (B)" of the Chinese Academy of Sciences (Grants XDB04040200), and Chinese Academy of Sciences (Grants KJCX2-EW-W11, KGZD-EW-303) are acknowledged.

REFERENCES

(1) Zhang, X.; He, J.; Chen, W.; Zhang, K.; Zheng, C.; Sun, J.; Liao, F.; Lin, J.; Huang, F. *Chem.—Eur. J.* **2014**, *20*, 5977−5982.
(2) Zhang, X.; Chen, W.; Mei, D.; Zheng, C.; Liao, F.; Li, Y.; Lin, J.; Huang, F. *J. Alloys Compd.* **2014**, *610*, 671−675.
(3) Liu, M.-L.; Chen, I. W.; Huang, F.-Q.; Chen, L.-D. *Adv. Mater.* **2009**, *21*, 3808−3812.
(4) Wang, Y.; Liu, M.; Huang, F.; Chen, L.; Li, H.; Lin, X.; Wang, W.; Xia, Y. *Chem. Mater.* **2007**, *19*, 3102−3104.
(5) Chan, G. H.; Liu, M.-L.; Chen, L.-D.; Huang, F.-Q.; Bugaris, D. E.; Wells, D. M.; Ireland, J. R.; Hersam, M. C.; Van Duyne, R. P.; Ibers, J. A. *Inorg. Chem.* **2008**, *47*, 4368−4374.
(6) Zheng, N.; Bu, X.; Wang, B.; Feng, P. *Science* **2002**, *298*, 2366−2369.
(7) Zheng, N.; Bu, X.; Feng, P. *Nature* **2003**, *426*, 428−432.
(8) Feng, P.; Bu, X.; Zheng, N. *Acc. Chem. Res.* **2004**, *38*, 293−303.
(9) Bu, X.; Zheng, N.; Li, Y.; Feng, P. *J. Am. Chem. Soc.* **2002**, *124*, 12646−12647.
(10) Zhang, Z.; Zhang, J.; Wu, T.; Bu, X.; Feng, P. *J. Am. Chem. Soc.* **2008**, *130*, 15238−15239.
(11) Zheng, N.; Bu, X.; Vu, H.; Feng, P. *Angew. Chem., Int. Ed.* **2005**, *44*, 5299−5303.
(12) Manos, M. J.; Jang, J. I.; Ketterson, J. B.; Kanatzidis, M. G. *Chem. Commun.* **2008**, 972−974.
(13) Feng, M.-L.; Kong, D.-N.; Xie, Z.-L.; Huang, X.-Y. *Angew. Chem., Int. Ed.* **2008**, *47*, 8623−8626.
(14) Li, J.-R.; Huang, X.-Y. *Dalton Trans.* **2011**, *40*, 4387−4390.
(15) Zhang, R.-C.; Yao, H.-G.; Ji, S.-H.; Liu, M.-C.; Ji, M.; An, Y.-L. *Chem. Commun.* **2010**, *46*, 4550−4552.
(16) Manos, M. J.; Malliakas, C. D.; Kanatzidis, M. G. *Chem.—Eur. J.* **2007**, *13*, 51−58.
(17) Manos, M. J.; Chrissafis, K.; Kanatzidis, M. G. *J. Am. Chem. Soc.* **2006**, *128*, 8875−8883.
(18) Manos, M. J.; Iyer, R. G.; Quarez, E.; Liao, J. H.; Kanatzidis, M. G. *Angew. Chem., Int. Ed.* **2005**, *44*, 3552−3555.
(19) Yaghi, O. M.; Sun, Z.; Richardson, D. A.; Groy, T. L. *J. Am. Chem. Soc.* **1994**, *116*, 807−808.
(20) Li, H.; Kim, J.; Groy, T. L.; O'Keeffe, M.; Yaghi, O. M. *J. Am. Chem. Soc.* **2001**, *123*, 4867−4868.
(21) Zheng, N.; Bu, X.; Feng, P. *J. Am. Chem. Soc.* **2005**, *127*, 5286−5287.
(22) Rumble, J.; Vaqueiro, P. *Solid State Sci.* **2011**, *13*, 1137−1142.
(23) Vaqueiro, P. *Inorg. Chem.* **2007**, *47*, 20−22.
(24) Mertz, J. L.; Ding, N.; Kanatzidis, M. G. *Inorg. Chem.* **2009**, *48*, 10898−10900.
(25) Cahill, C. L.; Ko, Y.; Parise, J. B. *Chem. Mater.* **1998**, *10*, 19−21.
(26) Li, H.; Laine, A.; O'Keeffe, M.; Yaghi, O. M. *Science* **1999**, *283*, 1145−1147.
(27) Cahill, C. L.; Parise, J. B. *J. Chem. Soc., Dalton Trans.* **2000**, 1475−1482.
(28) Su, W.; Huang, X.; Li, J.; Fu, H. *J. Am. Chem. Soc.* **2002**, *124*, 12944−12945.
(29) Li, H.; Kim, J.; O'Keeffe, M.; Yaghi, O. M. *Angew. Chem., Int. Ed.* **2003**, *42*, 1819−1821.
(30) Ding, N.; Chung, D.-Y.; Kanatzidis, M. G. *Chem. Commun.* **2004**, 1170−1171.
(31) Wu, T.; Wang, X.; Bu, X.; Zhao, X.; Wang, L.; Feng, P. *Angew. Chem., Int. Ed.* **2009**, *48*, 7204−7207.
(32) Wang, L.; Wu, T.; Zuo, F.; Zhao, X.; Bu, X.; Wu, J.; Feng, P. *J. Am. Chem. Soc.* **2010**, *132*, 3283−3285.
(33) Klepp, K. O.; Sing, M.; Boller, H. *J. Alloys Compd.* **1992**, *184*, 265−273.
(34) Zhang, X.; Kanatzidis, M. G.; Hogan, T.; Kannewurf, C. R. *J. Am. Chem. Soc.* **1996**, *118*, 693−694.
(35) Peplinski, Z.; Brown, D. B.; Watt, T.; Hatfield, W. E.; Day, P. *Inorg. Chem.* **1982**, *21*, 1752−1755.
(36) Liu, G.; Schulmeyer, T.; Brötz, J.; Klein, A.; Jaegermann, W. *Thin Solid Films* **2003**, *431*−*432*, 477−482.

DOI: 10.1021/acs.inorgchem.5b00317
Inorg. Chem. 2015, 54, 5301−5308

(37) Acharya, S.; Srivastava, O. N. *Phys. Status Solidi A* **1979**, *56*, K1−K4.
(38) Sheldrick, G. SHELXL-97, Program for crystal structure refinement. University of Göttingen: Germany, 1997.
(39) Kortüm, G.; Braun, W.; Herzog, G. *Angew. Chem., Int. Ed. Engl.* **1963**, *2*, 333−341.
(40) Perdew, J. P.; Burke, K.; Ernzerhof, M. *Phys. Rev. Lett.* **1996**, *77*, 3865−3868.
(41) Blochl, P. E. *Phys. Rev. B* **1994**, *50*, 17953−17979.
(42) Sunshine, S. A.; Kang, D.; Ibers, J. A. *J. Am. Chem. Soc.* **1987**, *109*, 6202−6204.
(43) Kanatzidis, M. G.; Park, Y. *J. Am. Chem. Soc.* **1989**, *111*, 3767−3769.
(44) Zhang, X.; Liu, Y.; Zhang, G.; Wang, Y.; Zhang, H.; Huang, F. *ACS Appl. Mater. Interfaces* **2015**, *7*, 4442−4448.
(45) Zhang, R.-C.; Yao, H.-G.; Ji, S.-H.; Liu, M.-C.; Ji, M.; An, Y.-L. *Inorg. Chem.* **2010**, *49*, 6372−6374.
(46) Schimek, G. L.; Kolis, J. W.; Long, G. J. *Chem. Mater.* **1997**, *9*, 2776−2785.
(47) Hayashi, A.; Noi, K.; Tanibata, N.; Nagao, M.; Tatsumisago, M. *J. Power Sources* **2014**, *258*, 420−423.
(48) Hayashi, A.; Noi, K.; Sakuda, A.; Tatsumisago, M. *Nat. Commun.* **2012**, *3*, 856.
(49) Yang, C.; Qin, M.; Wang, Y.; Wan, D.; Huang, F.; Lin, J. *Sci. Rep.* **2013**, *3*, 1286.
(50) Tripathi, R.; Gardiner, G. R.; Islam, M. S.; Nazar, L. F. *Chem. Mater.* **2011**, *23*, 2278−2284.
(51) Kim, S. K.; Mao, A.; Sen, S.; Kim, S. *Chem. Mater.* **2014**, *26*, 5695−5699.
(52) Hayashi, A.; Hama, S.; Morimoto, H.; Tatsumisago, M.; Minami, T. *Chem. Lett.* **2001**, *30*, 872−873.
(53) Bohnke, O.; Ronchetti, S.; Mazza, D. *Solid State Ionics* **1999**, *122*, 127−136.
(54) Irvine, J. T. S.; Sinclair, D. C.; West, A. R. *Adv. Mater.* **1990**, *2*, 132−138.

DOI: 10.1021/acs.inorgchem.5b00317
Inorg. Chem. 2015, 54, 5301−5308